UNIVERSITY OF AMSTERDAM

UvA-DARE (Digital Academic Repository)

Angle-resolved cathodoluminescence nanoscopy

Coenen, T.

Publication date
2014

Link to publication

Citation for published version (APA):
Coenen, T. (2014). *Angle-resolved cathodoluminescence nanoscopy*. [Thesis, externally prepared, Universiteit van Amsterdam].

General rights
It is not permitted to download or to forward/distribute the text or part of it without the consent of the author(s) and/or copyright holder(s), other than for strictly personal, individual use, unless the work is under an open content license (like Creative Commons).

Disclaimer/Complaints regulations
If you believe that digital publication of certain material infringes any of your rights or (privacy) interests, please let the Library know, stating your reasons. In case of a legitimate complaint, the Library will make the material inaccessible and/or remove it from the website. Please Ask the Library: https://uba.uva.nl/en/contact, or a letter to: Library of the University of Amsterdam, Secretariat, P.O. Box 19185, 1000 GD Amsterdam, The Netherlands. You will be contacted as soon as possible.

UvA-DARE is a service provided by the library of the University of Amsterdam (https://dare.uva.nl)

Download date:04 Nov 2026

10

Variable modal excitation efficiency in plasmonic dolmens through nanoscale electron beam positioning

Plasmonic "dolmen" metamolecules support coupled monomer and dimer modes which can interfere to giving rise to distinct resonant scattering phenomena. In this Chapter we study the nanoscale interplay between localized modes in gold dolmens using a combination of cathodoluminescence and electron energy-loss spectroscopy and resolve the degree of radiative character of these modes on the nanoscale. We perform a systematic comparison of dolmens with different sizes and geometries and explain the relevance of different driving positions. By precisely controlling the excitation position we are able to control modal amplitudes which can be used to tailor emission spectra with a great degree of accuracy.

10.1 Introduction

Plasmonic nanostructures have gained significant interest due to their ability to manipulate light on the nanoscale. Plasmonic resonances in nanoparticles can be tuned by their shape, size, and dielectric environment. By combining particles into composite structures one gains additional tunability which can be utilized to engineer *e.g.* highly directional antennas [39, 186]. Furthermore one can combine

particles into "metamolecule" configurations with unique near-and far-field optical properties. Analogous to real molecules, the relative orientation and position of the constituent elements has an important influence on the overall resonant properties. Plasmonic metamolecules can exhibit Fano interference where two modes, typically a high-Q subradiant mode and a low-Q superradiant mode, interfere to yield a Fano lineshape. In some cases this leads to a plasmon-induced transparency (PIT) [121, 239–246]. Such Fano resonances can be engineered to be highly dispersive, which makes them attractive for various types of optical sensing schemes [44, 45, 242, 247, 248].

A particular type of metamolecule which has been studied extensively in the literature is the "dolmen" or "π" structure in which a nanorod is capacitively coupled to an orthogonally oriented dimer composed of two vertical nanorods [239–241, 249, 250]. The monomer rod supports a strongly scattering dipole resonance that couples to a subradiant quadrupolar type resonance in the dimer. Depending on the spacing of the elements, *i.e.* the degree of near-field coupling between the elements, and the resonance detuning, the interference between these two modes can lead to a PIT transmission window in the visible/NIR regime, in which the transmission is near-unity. Counterintuitively, the local fields on the dimer are very strong within this transparency window while the extinction is low. This makes the dolmen antennas interesting for coupling to local emitters or for enhancing nonlinear effects. The dolmen scattering behavior can be well understood using a coupled harmonic oscillator model [239, 241]. In fact, this coupling phenomenon is generic and can occur for any type of coupled oscillator system. For instance, a localized surface plasmon resonance (LSPR) coupled to a light-emitting waveguide mode also gives a transparency window in transmission while the local fields in the waveguide are very strong, allowing fluorescence enhancement within this window [251]. Similarly, it has been shown that there can be enhanced absorption within a window of suppressed scattering for various coupled systems [252, 253].

Although dolmens have been studied extensively in arrays with plane-wave excitation, to fully exploit their potential, in *e.g.* sensing and spontaneous emission control, it is important to investigate how individual structures respond to a local excitation source. Cathodoluminescence (CL) spectroscopy and electron energy-loss spectroscopy (EELS) provide powerful platforms for studying the local response of composite plasmonic nanostructures owing to the high spatial resolution and broadband spectral characteristics of the electron beam excitation [67, 88, 197, 245, 254–256]. In this Chapter we study the local response of gold plasmonic dolmen structures using EELS and CL. In particular, we study the influence of size and particle separation on the scattering behavior and we investigate how the coupling between the elements manifests itself in the near field. To compare the experimentally studied local response to the plane-wave response, we use finite-difference time-domain (FDTD) simulations. The CL and EELS measurements are performed on the same structures so that we can directly compare the two techniques, enabling a differentiation between "dark" and "bright" dimer modes for example.

10.2 Dolmen geometry and fabrication

The dolmen structure consists of a horizontal monomer coupled to a vertical dimer. A schematic representation of the experiment and the structure is shown in Fig. 10.1(a). Using a beam of fast electrons (300 keV for EELS and 30 keV for CL experiments) we can locally excite the dolmen structure. During this excitation process the electrons transfer energy to the structure which can be detected in an electron energy-loss spectrometer (see Section 2.5). This excitation can subsequently couple out as far-field radiation which can be collected by our CL system (see Section 2.2 for details). The EELS and CL measurements were performed in different electron microscopes although simultaneous collection is also possible in principle. The EELS experiments were performed at Stanford University in the group of professor Mark Brongersma with the help of David Schoen.

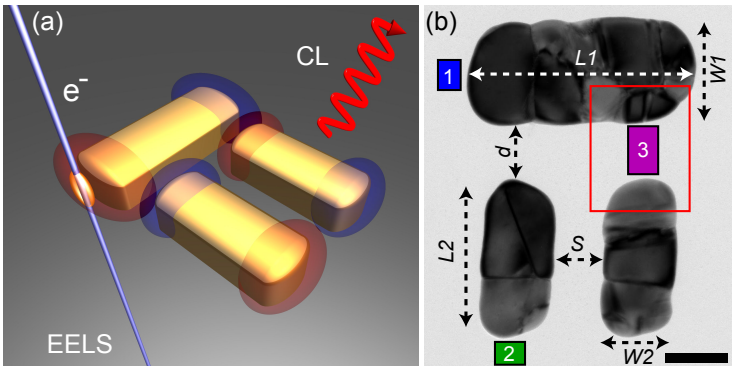


Figure 10.1: (a) Schematic representation of the experiment. Fast electrons excite the structure during which they experience energy loss which can be measured by EELS in a TEM. The excitation can be coupled out as far field radiation (CL) which can be collected by our CL system (b) Bright-field transmission electron micrograph of a gold dolmen structure of size 2 (see Table 10.1). In the image we have indicated the different size parameters. The blue, green, and magenta boxes indicate regions of interest that are referred to throughout the chapter. The red box indicates which part of the image is used for Fig. 10.5(a). The scaler bar represents 50 nm.

In order to perform EELS experiments an electron-transparent substrate is needed. To that end we fabricated gold dolmens on 15 nm thick Si_3N_4 membranes using a combination of electron beam lithography (EBL), thermal evaporation, and lift-off (see Supplementary Section 10.9.1 for details). Although the CL experiments do not require an electron transparent substrate, they do benefit from having such a thin membrane as substrate as this nearly fully eliminates background radiation. We fabricated three sizes of dolmens (see Table 10.1 for exact dimensions). For the smallest dolmen size we also varied the spacing between the monomer and

dimer in order to vary the near-field coupling between the two. Additionally, we have fabricated individual bars and dimers as references for each dolmen size. Figure 10.1(b) shows a bright field (BF) transmission electron micrograph of a dolmen structure of size 2. In the image we have indicated the different in-plane geometrical parameters that define the dolmen geometry. To determine the height of the structures we used atomic force microscopy (AFM) measurements (see Supplementary Fig. 10.8). In Fig. 10.1(b) we have also specified three regions of interest (ROI) to which we will refer throughout this Chapter. Although we have drawn only one box here per ROI we use two (on left and right side) to improve the signal-to-noise ratio in the spectra where we benefit from the fact that the dolmen is mirror symmetric across the vertical axis.

10.3 Single nanorods and dimers

To investigate the response of the dolmen structure we first study its constituent building blocks. To that we end we measured spatially resolved CL and EELS spectra on individual rods and dimers (for details on the experimental parameters see Supplementary Section 10.9.2). We raster-scan the electron beam in small steps over the structure and at each position we measure a EELS/CL spectrum. As the gold layer is quite thick (~40 nm, see Supplementary Fig. 10.8), the EELS signal that is measured through the metal does not uniquely represent the optical resonances as other inelastic processes occurring in the dense gold layer also cause energy loss. Hence we only take into account the excitation positions where the beam does not directly hit the structure. Because the evanescent electromagnetic fields extend away from the electron trajectory it can still couple in this "aloof" excitation configuration, while it does not experience collisions in the gold nanostructure. For CL measurements we do not have this restriction because we only measure the far-field emission and do not need to preserve the primary electron beam quality.

Figure 10.2(a) shows the spatially integrated CL and EELS spectrum for a single gold rod with dimensions of size 2. An annular-dark field (ADF) scanning transmission electron microscopy (STEM) image of the structure is shown as inset. We clearly observe two peaks in the spectra which correspond to LSPRs in the structure. To identify these resonances we simulate the scattering (Q_{scat}) and absorption cross section (Q_{abs}) (normalized to the geometrical cross section) for plane-wave excitation with the polarization along and transverse to the long axis of the rod, using total-field scattered-field simulations in FDTD [232] (for details see Supplementary Section 10.9.3). The simulation results are shown in Fig. 10.2(b). For polarization along the long axis we observe a peak in the scattering at λ_0 = 860 nm while for transverse polarization a peak is observed at λ_0 = 620 nm. Both resonances have cross sections that significantly exceed the geometrical cross section of the particle, as is often the case for LSPRs. As insets we also plot the real part of the out-of-plane electric field component (E_z) of the induced near-field (at the middle of the rod, h = 20 nm) which clearly reveals that we are driving transverse

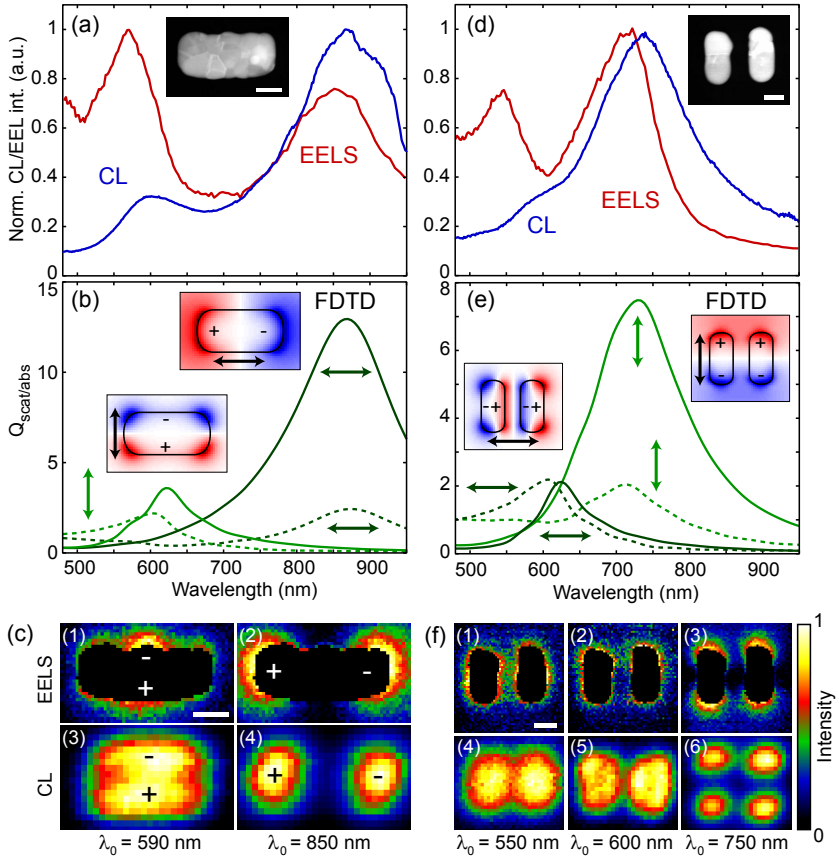


Figure 10.2: Spatially integrated CL and EELS spectrum of (a) a single gold rod and (d) dimer with similar dimensions to the the dolmen from Fig. 10.1. ADF STEM images of the structures are shown as insets. (b,e) Scattering (solid curves) and absorption (dashed curves) cross section simulations for the single bar and dimer for two orthogonal polarizations as indicated by the arrows, calculated using a TFSF source in FDTD. The cross sections have been normalized by the geometrical cross sections of the structures. As insets we show the corresponding E_z near field distributions, revealing the transverse and longitudinal dipole resonances. (e) EELS and CL spatial excitation distributions for single bar for λ_0 = 550, 600, and 850 nm corresponding to transverse and longitudinal dipole resonances. (f) EELS and CL spatial excitation distributions for dimer for λ_0 = 550, 600, and 750 nm. Scale bars correspond to 50 nm.

(blue peak) and longitudinal electric dipole resonances. The transverse resonance is blue-shifted with respect to the longitudinal resonance because the conduction electrons experience a larger restoring force due to the reduced width.

The simulated scattering cross section spectrum qualitatively matches the in-

tegrated CL data, where the resonance wavelengths, linewidths, and relative peak heights are well-reproduced. In contrast, while the EELS spectrum shows similar peak wavelengths and linewidths, the transverse resonance is stronger than the longitudinal resonance, contrary to the CL and FDTD simulations. This can be explained by the following effects. First, the FDTD absorption cross sections for the two resonances are close in magnitude and roughly follow the scattering cross section, but the relative amount of absorption compared to the scattering is larger for the transverse resonance which should lead to an increased peak height in EELS. Furthermore the degree of field confinement is higher for the transverse resonance so any absorbing layer like a contamination layer or the germanium seed layer will increase the absorption more for this resonance compared to the longitudinal mode, leading to a larger difference in EELS and CL. We note that for the transverse resonance the CL and EELS data are slightly blue-shifted compared to the FDTD. It has been suggested that one might expect a red-shift in the EELS measurement, compared to an optical experiment because the near-field should be redshifted compared to the far-field [257]. Thus far it has not been resolved in literature whether CL and EELS measurements are generally blue-shifted or redshifted with respect to each other or compared to optical data and it highly depends on the experiment and structure what is observed [258, 259]. For comparison with optical simulations, differences in the exact sample geometry and optical constants are a major factor but there are several other effects as well that can influence the experimentally measured spectral positions like charging and carbon deposition as explained in detail in Ref. [259].

By studying the spatial profiles we can verify the nature of the observed resonance peaks. Figure 10.2(c) shows the 2D EELS and CL excitation maps at two resonance wavelengths. As the electron beam preferentially couples to E_z components [63], an electrical dipole resonance will be excited efficiently at the particle extremities along the dipole axis as there is a strong E_z component at those positions (see the field profiles in Fig. 10.2(b) and CL maps in Fig. 5.2(b,d,e)) [260]. Indeed, the EELS and CL maps clearly show such features, consistent with the excitation of transverse and longitudinal resonances.

Next, we perform a similar analysis for the isolated dimer structure. The response of a single dimer rod is not shown here as it is similar to what is shown in Fig. 10.2(a-c) but blueshifted because of the smaller in-plane dimensions. Figure 10.2(d) shows the spatially integrated CL and EELS spectra for the dimer. Again, two peaks are clearly visible in the spectra. The short-wavelength peak is quite weak for CL and appears as a shoulder around λ_0 = 600 nm whereas for EELS it is much more pronounced and centered around λ_0 = 550 nm. The FDTD field plots in the inset of (e) shows that plane-wave excitation drives a transverse and longitudinal dipole modes with the rods excited in phase. The blueshift of both peaks compared to the spectra for the individual larger rod is due to the abovementioned size difference. Compared to a single dimer rod however, these collective dimer modes are redshifted for the transverse mode and blueshifted for the longitudinal mode respectively (not shown here). This can be understood from a hybridization scheme

were the transverse mode is energetically favorable (bonding) and the longitudinal mode is energetically unfavorable due to the charge distributions associated with these modes (see hybridization schemes in Fig. 10.10(a,b)) [261, 262].

For the dimer it is less straightforward to directly compare the plane-wave case to the CL and EELS spectra and excitation maps like we could for the single rod. The dimer also supports an antibonding mode for transverse excitation and a bonding mode for longitudinal excitation, where the dipole moments in the rods are in anti-phase (see Supplementary Fig. 10.10(a,b)). These modes are symmetry-forbidden for plane-wave excitation under normal incidence [263–265] but can be accessed with local electron beam excitation [72, 88, 254, 260, 266]. Hence the peaks observed in CL/EELS could be due to four modes rather than two.

Next, we use the spatial profiles in Fig. 10.2(f)) to identify which modes are responsible for the peaks observed in the EELS and CL data. For the blue peak in EELS at λ_0 = 550 nm (excitation map (1)) we observe excitation hotspots along the short axis of the rods and a high excitation probability in the gap region between the two rods, whereas at 600 nm (excitation map (2)) the excitation probability is significantly lower in the gap region. In the bonding mode there is destructive interference of the E_z component in the center of the gap (clearly visible in the FDTD E_z field profile for this mode in Fig. 10.2(e)), so a low excitability is expected at that position whereas for the antibonding mode there is constructive E_z interference leading to a high excitability in the gap region [72, 254, 260, 266]. Therefore we conclude that map (1) is consistent with the transverse antibonding mode and map (2) is consistent with the transverse bonding dimer mode. The position of the peak in CL coincides with the peak in FDTD for the bonding mode and also the spatial profile matches well. The blueshifted antibonding mode most likely does not radiate efficiently and therefore its contribution to CL is small compared to the EELS spectrum. We note that the vertical z-dipole mode in the rods, which peaks around λ_0 = 510 nm for a single rod without membrane (not shown here), could play a role in explaining the discrepancy between the EELS and CL signal as well, as this resonance has a low albedo due to the high degree of confinement along the z-axis, and thus may appear more strongly in the EELS.

We will now discuss the longitudinal dimer modes which are most relevant for the canonical dolmen PIT behavior. We observe no noticeable peak-splitting in the longitudinal resonance peak around λ_0 = 750 in Fig. 10.2(d) suggesting a relatively weak coupling between the rods for the longitudinal case. This could be due to the fact that the field overlap between the rods is rather small in this configuration, which is corroborated by the EELS and CL maps for this wavelength (maps (3,6) in in Fig. 10.2(f)) which shows that there is poor spatial overlap between the excitation hotspots. When the rods are brought close enough ($S < 1$ nm) this splitting can become substantial such that separate peaks are visible as was shown in Ref. [264].

The EELS and CL maps of the dimer for the peak at λ_0 = 750 nm (maps (3,6) in Fig. 10.2(f)) show that that excitation probability is highest at the rod apices but such behavior is expected for both the bonding and antibonding longitudinal modes. However, there should be a subtle difference between the two. For the

antibonding mode the rods are in phase leading to constructive E_z interference in the gap region near the apices (also clear in FDTD E_z profile for this mode in (e)). As a consequence we expect that we can drive that mode in the gap region as well whereas for the bonding mode that is not be possible because there is no E_z component present. In our case the maps are more consistent with the latter case. Supplementary Fig. 10.11 shows the EELS spectra for excitation within the gap and at the apices. From the spectra it is clear that at the apices the spectrum is slightly redshifted compared to within the gap. This effect is also apparent in the spatial EELS profiles in the range λ_0 = 650 to 750 nm where the gap region gradually becomes darker for increasing wavelength (see maps (1-3) in Supplementary Fig. 10.11(b)). These observations suggest that the peak at λ_0 = 750 nm in Fig. 10.2(d) is due to two modes, where the excitation efficiency of the antibonding mode decreases relative to the bonding mode for increasing wavelength.

To verify this hypothesis we perform FDTD simulations where we placed a vertically-oriented electrical point-dipole source at the apex of one of the rods and plotted the resulting E_z field profiles (Fig. 10.11(b)). The driving field of the dipole has not been removed from the image which means that images show a mix of the driving field and the induced field on the dimer. In order to see the induced fields on the dimer the colorscale has been saturated by a factor 300. As is clear from maps 3 and 6 in Fig. 10.2(f) the CL and EELS signal is highest at the apices of the rods for this wavelength, so the spectral contribution from these spots is largest. If a point dipole is placed in one of these hotspots the near-field patterns show that it is predominantly driving one the rods which, through capacitive near-field coupling, induces an opposite dipole moment in the other rod, suggesting that the longitudinal bonding dimer mode is dominant in our experiment. Using the knowledge we have about the individual elements we can now attempt to understand the dolmen response.

10.4 Inter-particle coupling in the dolmen

Figure 10.3(a,b) show spectra measured on a dolmen of size 2 at ROI 1 and 2. At ROI 1 we efficiently drive the longitudinal dipole mode in the top bar. From previous optical experiments, it is known that this monomer mode can couple to the bonding dimer mode [239–241, 249, 250] so possibly we can observe coupling between dimer and monomer at this position. The EELS and CL spectra show three peaks at this excitation position while in the reference monomer in Fig. 10.2(a) we only observe two peaks. At ROI 2 we only observe one main peak at λ_0 = 750 nm, matching the spectral position of the extra feature for ROI 1, showing that this additional spectral feature is related to coupling with the dimer. Similar to the data for the individual monomer and dimer, the EELS data is more pronounced in the blue compared to the CL data. We know that the dolmen can support a low-energy bonding and a high-energy antibonding mode (see Supplementary Fig. 10.10). Because the dimer mode and monomer mode are detuned and relatively weakly coupled, the

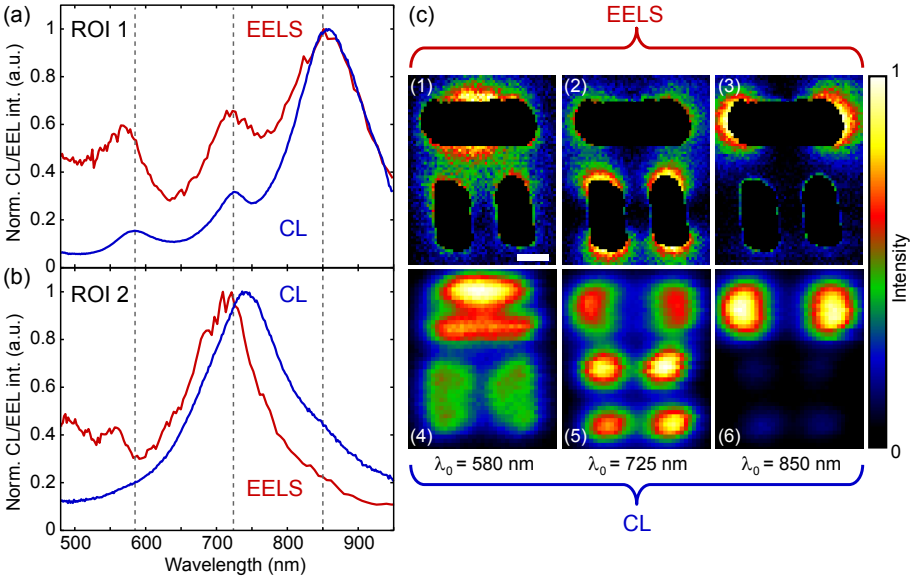


Figure 10.3: (a) CL (blue) and EELS (red) spectrum for excitation position 1 for the dolmen shown in Fig. 10.1c. For this excitation position the top bar is directly driven. (b) CL and EELS spectrum for excitation position 2 where we directly drive on of the dimer rods. (c) 2D EELS (images 1 – 3) and CL (images 4 – 6) for λ_0 = 590, 725, and 850 nm respectively, integrated over a 30 nm bandwidth. Scale bar is 50 nm.

hybridized bonding and antibonding modes are close in frequency to those for the bare dimer and monomer states, where the bonding mode has more monomer character and the antibonding mode has more dimer character.

As is explained in Ref. [255] the electron beam excitation is markedly different from plane-wave excitation in the case of such metamolecules. The electron energy-loss probability is determined by the near field acting back on the electron at the impact position [63]. In this case the near field of the entire structure acts back on the excitation positions at ROI 1 and 2. At ROI 1 the monomer is directly excited and the dimer can flip its phase relative to the monomer depending on whether the wavelength is below or above the dimer mode resonance wavelength. In other words, the wavelength with respect to the bonding dimer resonance position determines whether it is excited in-or out-of-phase with the driving field that is mediated by the monomer. Hence, both the bonding and antibonding dolmen mode can be driven at this position and act back on the electron which is the reason why we observe an additional peak in the EELS and CL spectrum. *Vice versa*, at ROI 2 we directly drive the dimer mode and the phase of the monomer can flip depending on the frequency.

The effects mentioned above are visible in the spatial maps in Fig. 10.3(c) for

the three peak positions. For the peak at λ_0 = 850 nm, the excitation efficiency is highest on the monomer-ends similar to the individual monomer illustrating that is this mode has strong monomer character (maps (3,6)), whereas the mode at λ_0 = 725 nm (maps (2,5)) has more dimer character. This is consistent with the fact that at the these wavelengths the dimer is forced into the bonding and antibonding configuration respectively, due to its in/out-of-phase response with respect to the driving field. The excitation efficiency of the antibonding mode does not decline as one moves towards the top of the monomer. From this we conclude that the dimer excitation is indeed mediated by the monomer and does not occur directly through the evanescent electron fields, for which a rapid signal decay is expected away from the structure as is visible in the reference dimer spatial maps (Fig. 10.2(f), maps (3,6)).

Further proof that the peaks at λ_0 = 850 and 725 nm correspond to the bonding and antibonding dolmen modes can be given by studying the excitation efficiencies in the gap between monomer and dimer for the two wavelengths. In maps (3,6) the gap between dimer and dolmen is dark due to the destructive E_z near-field interference for the bonding mode, whereas in maps (2,5) the gap is significantly brighter, consistent with the antibonding dolmen mode where the interference is constructive. Interestingly, we observe that for λ_0 = 850 nm the excitability is higher on the bottom of the dimer than on top, suggesting that bonding dolmen mode can be excited more efficiently from this position, although the effect on the spectrum seems to be small.

Because the coupling between dimer and monomer is relatively weak and the peaks both are quite broad spectrally we do not observe a clear Fano feature/PIT window. Also the spectral shift of the hybridized bonding and antibonding dolmen modes, compared to the bare dimer and monomer is not large enough to be clearly resolved, as the experimentally observed spectral shifts are also influenced by small size/shape differences in the dolmen elements, inherent to the EBL fabrication process. We expect that for more strongly coupled systems one could potentially resolve these features [255]. FDTD simulations suggest that smaller spacings would bring the dolmens in this regime where the interference and modesplitting clearly start to manifest themselves in the spectra.

At λ_0 = 590 nm the transverse dipole resonance in the monomer is dominant, as is clearly visible in maps (1,4). This state can hybridize with the antibonding dimer mode (see Supporting Fig. 10.10(d)) [240]. For our geometry these modes are detuned significantly so we do not observe any extra features in the spectrum related to modal coupling, like we could for the other modes at λ_0 = 725 nm and λ_0 = 850 nm.

10.5 Size-dependent optical response

It is well-known that plasmonic resonances redshift for increasing particles size. Here we investigate how the dolmen response scales with size. Figure 10.4(a) shows EELS and CL spectra taken at ROI 1 for the three fabricated dolmen sizes. Clearly, all spectral features move towards the red as the size increases, although the exact detuning between dimer and top bar varies somewhat for each size. For each size we observe coupling from the monomer to the dimer at ROI 1. On the right side of the figure we also show the EELS and CL excitation maps for the central antibonding dolmen peak for each size at λ_0 = 675, 730, and 790 nm for size 1, 2 and 3 respectively. Like the spectra, the spatial profiles remain very similar as the size increases. For the smallest size dolmen the excitation positions on the particles were not masked in the EELS spatial maps because the metal is substantially thinner (see Supplementary Fig. 10.8) and the EELS signal better reflects the optical modes that are excited. For the smallest dolmens the CL data is significantly red-shifted compared to the EELS data. We noticed that during the CL scan the response redshifted while the quality factor remained roughly constant which is an indication that there is local deposition of a carbonaceous contamination layer during electron beam scanning. Such *in-situ* redshifting was not observed in the measurements for other sizes which either means that the contamination level was different on that sample or that the larger structures are simply less sensitive to a thin contamination layer.

Figure 10.4(b) shows the plane-wave scattering and absorption cross section for horizontal polarization along the monomer for each of the dolmen sizes, calculated using FDTD. Also here the features redshift and for each size we observe a modest transparency window (indicated by the gray dashed line). If one decreases the spacing the modal splitting and modulation depth of the window can be substantially increased (not shown here). To show that this transparency window is similar to those discussed in literature we show the induced E_z near-field distribution at the PIT wavelength, for each of the sizes in the first column on the right of Fig. 10.4(b). We clearly see the reduced intensity on the monomer and the antisymmetric charge distribution in the dimer. In the plane-wave case the transverse mode in the dimer is also driven simultaneously unlike in the CL/EELS experiment, which leads to an increased contribution around λ_0 = 600 nm. To demonstrate that the well-known hybrid dolmen modes can also be driven when locally excited by a point-like source we show the near-field patterns for dipole excitation at ROI 1 as well (see second column in Fig. 10.4(b)). In this case we could not subtract the incident field like we could for the plane wave which distorts the pattern relative to the unperturbed eigenstate. Nevertheless we can clearly recognize the characteristic antisymmetric dimer mode in all dolmen sizes, suggesting that this type of driving excites the same modes as horizontally polarized plane-wave excitation.

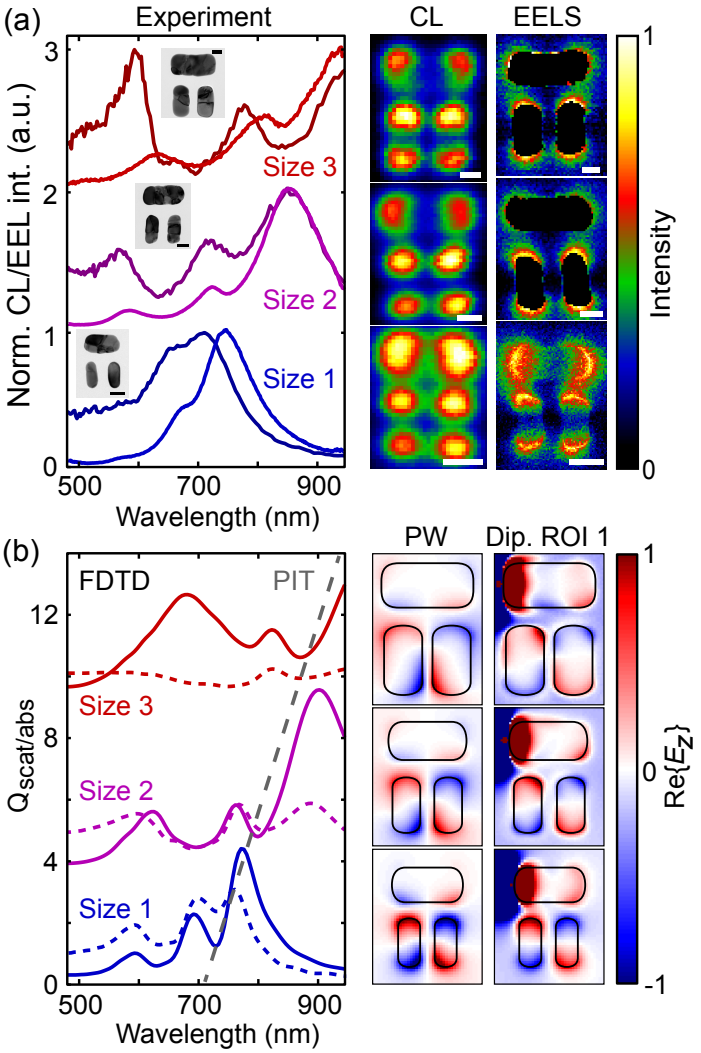


Figure 10.4: (a) EELS (dark curves) and CL spectra (bright curves) at excitation position 1 for all dolmen sizes. The spectra have been vertically offset for clarity. The corresponding BF TEM images are shown as insets. The EELS and CL spatial maps at the central peak, corresponding to the antibonding dolmen mode, are shown on the right (at λ_0 = 675, 730, and 790 nm for size 1, 2 and 3 respectively). (b) Normalized scattering (solid curves) and absorption (dashed curves) cross sections of dolmen structures for polarization along the top bar, calculated by FDTD. The spectra have again been vertically offset for clarity. The PIT feature indicated by the gray dashed line shifts with size towards the red. First column on the right shows the E_z near field distribution at the PIT window for plane-wave excitation (PW) (λ_0 = 730, 750, and 880 nm for size 1, 2 and 3 respectively). Second column shows the same maps for vertical point dipole excitation 10 nm left of the top bar (ROI 1) at half-height of the rod.

10.6 Variable modal excitation efficiency

Thus far we have focused on ROIs 1 and 2 where just one of the dolmen elements is directly excited by the beam. Next, we investigate the region between the monomer and one of the dimer rods (ROI 3), where simultaneous driving of the dolmen elements is possible. The area of interest is indicated by the multicolored box in the TEM image in Fig. 10.5(a), which itself is a blow-up of the area enclosed by the red box in Fig. 10.1(b)). Figures 10.5(b,c) show the CL and EELS spectra when the electron beam moves from the monomer towards the dimer rod (from top to bottom). The colors in the box in (a) are matched to the curve colors of the spectra in (b,c) and indicate the corresponding electron beam position in this direction. The width of the box (~30 nm) represents the lateral averaging range that we used in order to improve the signal-to-noise ratio.

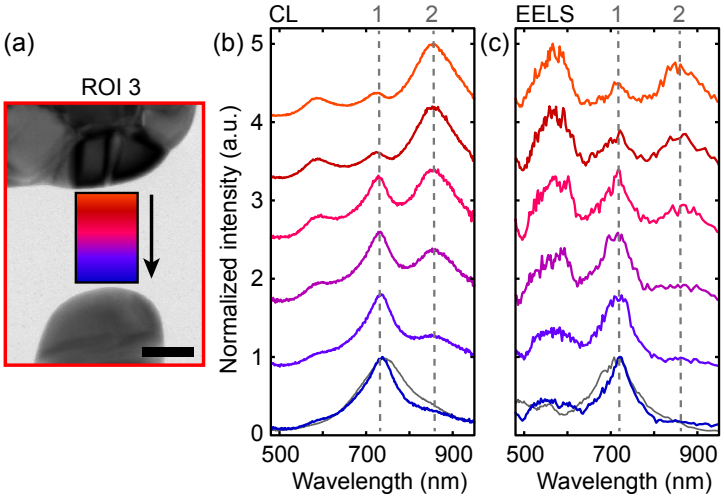


Figure 10.5: (a) BF TEM image corresponding to the area indicated by the red box in Fig. 10.1(b). (b,c) CL and EELS spectra scanning down from the top bar to the dimer (spectra match color code in box). We transversely average along the width of the box for a better signal-to-noise ratio. The gray curves on the bottom correspond to spectra collected at ROI 2. The spectra are vertically offset for clarity. Scale bar is 25 nm.

Clearly the spectra change completely while the electron position is varied by only 40 nm. In the following discussion we neglect the transverse monomer mode which is visible at λ_0 = 590 nm. Close to the monomer, the peak at λ_0 = 850 nm (peak 2) corresponding to the bonding dolmen mode is dominant. When moving towards the dimer, the peak at 750 nm (peak 1) corresponding to the antibonding dolmen mode starts to become stronger; close to the dimer it dominates the spectrum. Interestingly, this peak is more narrow than for ROI 2 (see Fig. 10.3) and

the subtle long-wavelength shoulder has disappeared. For comparison we have included the spectra for ROI 2 on the bottom (gray curves) of (b) and (c). We attribute this slightly different spectral shape to the fact that the bonding dolmen mode is inefficiently excited at this position due to destructive E_z near-field interference. This effect is also apparent from the spatial excitation maps 3 and 6 in Fig. 10.3(c) at the bonding mode wavelength (λ_0 = 850 nm), where a clear dark band is visible between dimer and monomer indicating a low excitation efficiency. For symmetric dimer structures this dark band usually is in the center in the gap as shown by others [72, 88, 254], but for our dolmen the monomer near field is stronger than that of the dimer at this wavelength, and as a result this band of low excitability shifts towards the dimer. This data shows that the spatial precision of electron beam excitation can be used to precisely tune the modal driving efficiency which is not possible for plane-wave excitation at normal incidence.

10.7 Varying intrinsic coupling strength

So far we have investigated the effect of size on the optical response and of changing the degree of modal driving by precisely controlling the excitation position. Next, we control the degree of intrinsic coupling between the dolmen elements. The coupling between monomer and dimer is mediated by the induced near fields in the nanorods which extend ~30 nm away from the structure. Hence, the intrinsic coupling strength is mainly determined by the spacing d between monomer and dimer. Figure 10.6(a,b) show CL and EELS spectra at ROI 1 and 2 for dolmens of size 1 with different spacings d = 30, 40, 50 and 60 nm. We have also included reference spectra from an individual reference monomer and dimer of this size ("$d = \infty$"). The spectra are vertically offset for clarity. For each separation distance the corresponding BF TEM image is shown on the right. The coupling between monomer and dimer is reflected by a shoulder in the EELS and CL spectra for ROI 1 around λ_0 = 675 nm for d = 30 nm. For d = 40 nm the shoulder is substantially lower and disappears completely for the dolmens with larger particle spacings, indicating that efficient coupling between dimer and monomer requires spacings smaller than 40 nm for this dolmen size.

Note that the main resonance positions also vary slightly from dolmen to dolmen without a clear trend, so we attribute these shifts to small size/shape variations in the dolmen elements. Figure 10.6 (c) show CL and EELS maps close to the antibonding dolmen mode spectral feature (λ_0 = 675 nm) for d = 60 nm (maps (1,2)) and d = 30 nm (maps (3,4)). Indeed, these maps show that there is significant field overlap in the case of d = 30, reflecting the efficient near-field coupling, while for d = 60 nm this overlap is much lower thereby preventing effective coupling between dimer and monomer.

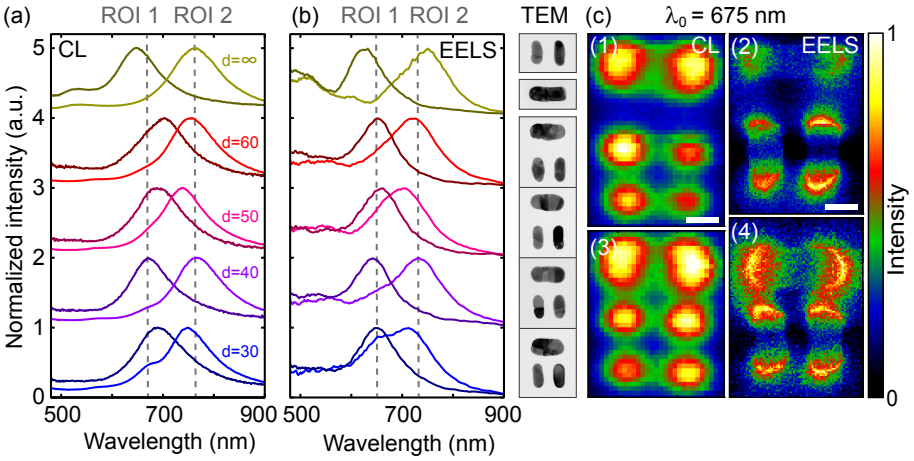


Figure 10.6: Change in coupling as function of distance d between top bar and dimer. (a) CL spectra and (b) EELS spectra for for excitation position 1 and 2 for size 1 at spacings d = 30, 40, 50 and 60 nm. We also show the reference single bar and dimer spectra ($d = \infty$). The spectra have been vertically offset for clarity. On the right side we show the corresponding BF TEM images of the structures. (c) CL (1,3) and EELS (2,4) maps for d = 30 and d = 60 nm at λ_0 = 675 nm.

10.8 Conclusions

In conclusion, we have used cathodoluminescence spectroscopy and electron energy-loss spectroscopy to study the local optical properties of dolmen metamolecules and their individual constituents in great detail. Taking advantage of the high spatial resolution we are able to spatially map the response of the dolmen to the local electron beam source. Additionally, this experiment provides an opportunity to directly compare electron energy-loss and cathodoluminescence signals. We find that the EELS response is stronger for higher energies compared to CL, related to the far-field scattering efficiency of the modes. In both EELS and CL experiments we clearly observe coupling between monomer and dimer in the near field. Furthermore we demonstrate that the dolmen spectral response redshifts for increasing size as is expected for plasmonic structures. The dimer-monomer coupling is a nanoscale near-field effect and we demonstrate that the intrinsic coupling strength can be tuned by changing the spacing. The local electron beam excitation also allows for simultaneous direct excitation of dolmen modes where their relative amplitude can be tuned by precise positioning of the beam. This type of metamolecule excitation allows tailoring of the emission spectrum in ways that cannot be achieved by plane-wave excitation.

10.9 Supplementary information

10.9.1 Sample fabrication on TEM membranes

We fabricated three sizes of gold plasmonic dolmen structures and reference structures on 3 × 3 mm TEM samples (Ted Pella Inc., USA) with nine 100 µm × 100 µm silicon nitride membranes (15 nm thickness) using a combination of EBL, thermal evaporation, and lift-off. For handling we attached the membrane chips to a 12 × 12 mm silicon chip. We spin a 145 nm thick layer of polymethyl methacrylate (PMMA) (at 3000 rpm for 45 seconds) onto the silicon support and heat it to 210 °C such that it becomes sticky. Subsequently we press the membrane chip into the PMMA (with Si_3N_4 side upward) and let it cool down for 10 minutes after which they are strongly attached (see step 1 in Fig. 10.7).

We then apply a hexamethyldisilazane (HDMS) primer (at 4000 rpm for 30 seconds) and ~150 nm of positive ZEP520A resist (at 2000 rpm for 45 sec) using a spincoater (step 2). We bake the sample for 1 minute at 180 °C after the HDMS step and 5 minutes after the ZEP520A step. Then we perform EBL in a Raith E-line system with 20 keV electrons using area-exposure at a dose varying between 20 – 250 µC/cm^2 (optimal dose between 90 – 130 µC/cm^2). The resist was developed by dipping the samples for 90 s in n-Amyl-acetate, 15 s in a 9:1 volume-ratio mixture of methyl isobutyl ketone and isopropyl alcohol, and 15 s in pure isopropyl alcohol (step 3). Subsequently we thermally evaporate 1 nm of germanium which acts both as adhesion layer and seed layer to reduce the metal granularity [228, 229] and a layer of gold (33 and 40 nm) for sample 1 and 2 respectively. We used an evaporation rate of 0.2 Å/s for the germanium and 0.5 Å/s for the gold at a base pressure of ~5 × 10^{-6} mbar.

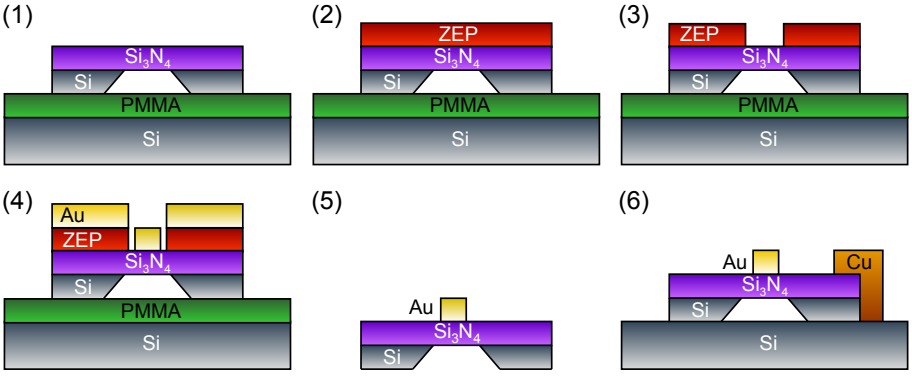


Figure 10.7: Schematic overview of the fabrication steps: (1) Attaching to silicon support using a PMMA resist layer. (2) Spinning of ZEP520A positive resist. (3) EBL and resist development. (4) Thermal evaporation of germanium and gold. (5) Lift-off in NMP. (6) Reattachment to silicon support with copper tape (for CL only).

Next, we lift off the excess metal by placing the sample in n-methylpyrollidone (NMP) at 65 °C for 3 hours (step 5). In this step the PMMA layer also dissolves thereby detaching the membrane chip from the support. This is necessary for the EELS measurements in the TEM. For the CL measurements we reattach the samples to a support using copper tape (step 6) to be able to clamp the sample in the SEM holder. After these processes we use a soft oxygen reactive-ion-etch (RIE) descum with low forward bias to remove any organic contaminations from the sample without damaging the structures or the membranes.

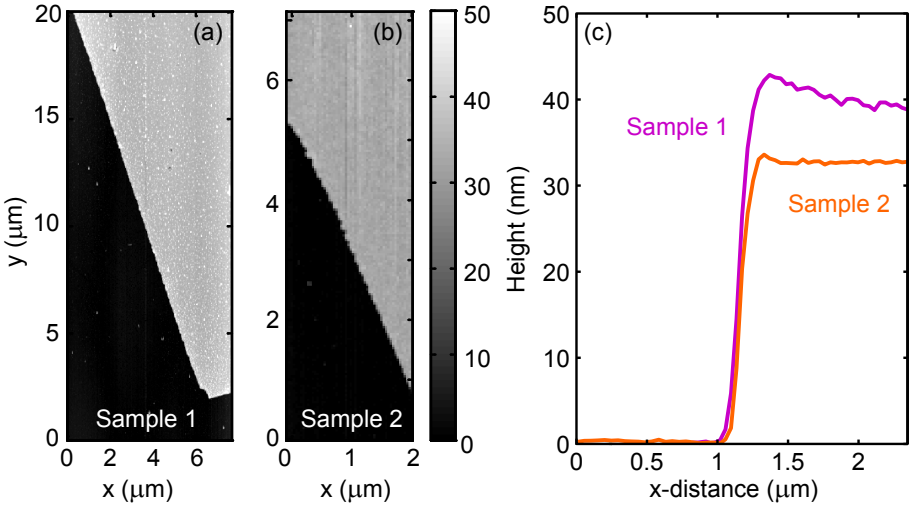


Figure 10.8: 2D AFM scans on reference gold pads on (a) sample 1 (dolmen size 2 and 3) and (b) sample 2 (dolmen size 1) where the grayscale indicates the height in nm. (c) Horizontal cross cuts along x for (a) and (b). We integrate over a 2 µm range in the y-direction and align the edge positions to obtain an average edge profile.

To characterize the metal thickness we use AFM measurements collected in tapping mode (Veeco Dimension 3100 AFM). Figure 10.8 shows AFM data taken on gold pads on sample 1 (dolmen size 2 and 3) and 2 (dolmen size 1). These gold pads are residuals from the electron beam focusing for the EBL process during which these parts of the resist where exposed to electron irradiation. These pads should have the same height as the gold antenna structures as they were created during the same evaporation session. The pads are on the silicon support making it possible to perform the AFM experiments without scanning the structures on the fragile membranes. The sizes of the dolmen structures are given in Table 10.1.

10.9.2 EELS and CL experiments

For more technical information on the CL and EELS setup we refer the reader to Sections 2.2 and 2.5 respectively. The CL measurements were performed in a FEI

Size	$L1$	$W1$	$L2$	$W2$	S	d	h
Size 1	125	60	90	40	30	30 – 60	33
Size 2	185	85	130	60	40	45	40
Size 3	215	100	160	90	30	45	40

Table 10.1: Dimensions of the dolmen structures for the three different sizes. The in-plane dimensions were derived from BF TEM data and the thickness from the AFM measurements. Dimensions are in nanometers.

XL-30 SFEG SEM equipped with a home-built CL-system. The measurements were done at 30 keV acceleration voltage and a beam current of 0.8 nA. The pixel size was 7.5, 8.5, and 10 nm for the three dolmen sizes respectively with an integration time of 0.5 s per pixel. With our CL system we have the capability to measure the angular pattern. However, due to the open geometry of the sample, the emitted light from the antenna can reflect off the bottom of the silicon support, other antennas on the membrane, or on the membrane edges which leads to substantial parasitic interference, thereby obscuring the emission pattern of the individual structure and making the angular measurements too unreliable.

The EELS measurements were taken in STEM mode at 300 kV acceleration voltage and a beam current of ~0.2 nA. During the EELS acquisition we simultaneously collect a STEM image using the annular dark field detector. To obtain a good reference we measure the zero-loss peak (ZLP) through a punctured membrane. For the final spectra we use a Richardson-Lucy algorithm to deconvolute the experimental EELS spectra with the ZLP which is considered to represent point spread function (PSF) of the system. The scanning pixel size was 3, 3.75, and 5 nm for the three dolmen sizes respectively with an integration time of 5 ms per pixel. In the EELS camera each pixel corresponds to an energy bandwidth of 0.01 eV. To transform the EELS intensity from per unit of energy to per unit wavelength like the CL data we multiply the data with the appropriate conversion factor: $100 \times hc/e\lambda_0^2$. In order to quantitatively compare the absolute EELS and CL signals one would need to account for the beam currents, integration times, and absolute system responses. Because we do not know all of these numbers we show normalized spectra which does allow direct comparison of the spectral shape. For all measurements shown here the EELS experiments were performed before the CL experiments.

10.9.3 FDTD simulations

To study the scattering properties of the dolmens and reference structures we carry out simulations of their optical scattering and absorption cross sections using finite-difference time-domain software [232]. For this we use a 3D "Total-Field Scattered-Field" (TFSF) source. A broad-band pulse (λ_0 from 400 – 1200 nm) is

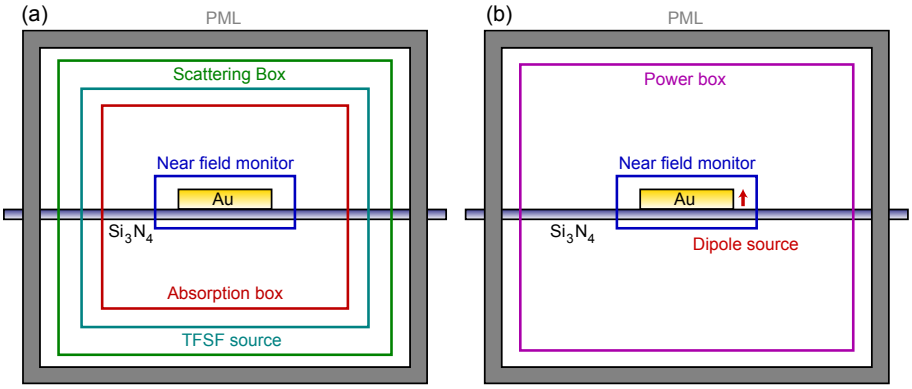


Figure 10.9: (a) Schematic of the FDTD simulation setup for the plane-wave TFSF simulations. The scattering box is used to calculate the scattering cross section whereas the absorption box can be used to calculate the absorption cross section. The near field monitor allows visualization of the induced near-fields on the structure. (b) Schematic of the FDTD setup for the point-dipole simulations. The power box collects the emitted power and the near-field monitor probes the near fields. In this case we cannot separate the driving field from the induced field.

used to simulate white light irradiation, incident on the structure from the top. The lateral dimensions of the structures are taken from TEM images and the thicknesses are taken from the AFM data. The membrane thickness is assumed to be 15 nm as specified by the manufacturer. The optical constants were taken from tabulated data for Au [114] and Si_3N_4. There are no free parameters in these simulations. In order to directly compare the dolmen simulations with the reference simulations on the monomers and dimers we assume that the references have exactly the same dimensions. In the experiments the particle sizes for the references differ slightly from the dolmen, which could give rise to small discrepancies between the simulated response and the experiments on the references. In the simulations, the particle shape is represented by a rectangular box with hemicylindroid end facets for the first two sizes. For the largest size the end facets are composed of an additional rectangular box sandwiched between two halves of a hemicylindroid. The scattering cross section is obtained by dividing the scattered intensity by the areal footprint of the structure. We simulate for two orthogonal incoming polarizations. To simulate the absorption in the structures we introduce a flux box inside the TFSF source. With a near field box we monitor the local near fields on the structure so that we can identify the responsible modes. Figure 10.9 shows a schematic of the simulation setup.

To mimic electron beam excitation we also simulate the response of the structure to a vertical point dipole source which is placed 10 nm away from structures at half-height of the gold antenna structure. In this case we cannot remove the driving fields from the near-field but nevertheless this procedure gives a good idea of the

induced fields on the structure. This simulation setup is shown in (b). To prevent scattered fields from the simulation boundaries we use perfectly matching layers (PMLs).

10.9.4 Hybridization schemes for dimer and dolmen

To understand the hybrid modes in our dolmen system it is useful to consider simple hybridization schemes [261]. The dimer consists of two nanorods. The longitudinal resonances in these rods can hybridize into a dipolar antibonding mode (which is energetically unfavorable because the charges at the apices repel each other) and bonding quadrupolar mode (see Fig. 10.10(a)). In the figure we show snapshots of the charge distribution at an arbitrary moment in time. Interestingly this antisymmetric charge-distribution is inaccessible for free space light at normal incidence due to its symmetry. We note that this mode has both electric quadrupole and magnetic dipole character [207]. In the context of dolmens it is usually referred to as "quadrupolar" mode whereas for cut-wire pairs it is often called "magnetic" mode.

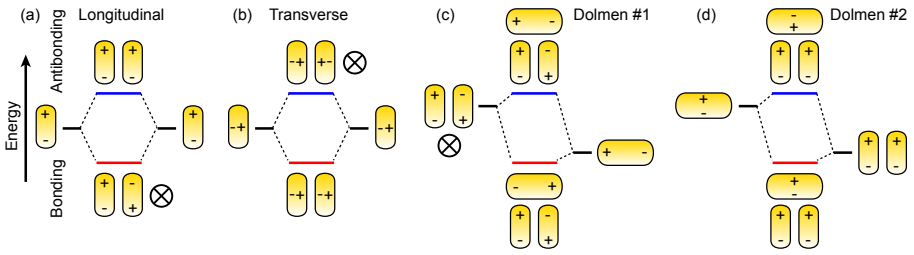


Figure 10.10: Hybridization schemes for (a) longitudinal dimer modes, (b) transverse dimer modes, (c) dolmen modes 1, and (d) dolmen modes 2. Each set of resonances hybridizes to give a set of bonding (lower energy) an antibonding modes (higher energy). In the case of the dolmen the hybridizing bare-state resonances are also detuned in frequency which leads to asymmetric mode splitting. The ⊗ symbol indicates that a mode is symmetry forbidden for plane-wave excitation at normal incidence.

For the transverse case (Fig. 10.10) the bonding mode can be driven efficiently with free-space light whereas the antibonding mode is symmetry forbidden at normal incidence. For off-normal incident light these symmetry-forbidden modes can be excited as that provides sufficient retardation [264]. With the electron beam all these modes can be excited where the excitation rate of each mode is determined by the electron beam position.

For the dolmen there are several hybridizations possible, depending on the size and aspect ratios of the rods. The most relevant for our experiment is the hybridization of the quadrupolar bonding mode in the dimer, which itself already is a hybridized state of two rods, with the longitudinal dipole mode in the horizontal

bar (Fig. 10.10(c)). The spectral measurements and FDTD measurements show that the monomer mode is redshifted compared to the dimer mode so the hybridization is not symmetric like is the case for the dimer. The second hybridization that could occur is between the transverse mode in the monomer and the dipolar antibonding mode in the dimer. In this case the transverse monomer mode is substantially blue-shifted compared to the dimer mode.

10.9.5 Discriminating longitudinal dimer modes

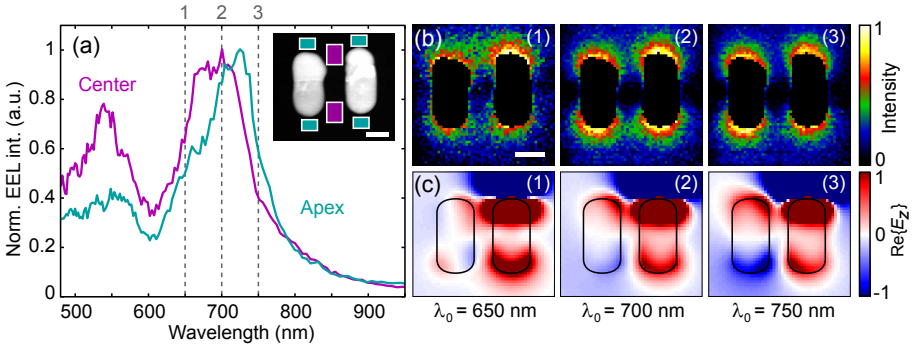


Figure 10.11: EELS spectra taken at the apices (cyan curve) and in the center (magenta curves) of the size 2 dimer. The spectral collection areas are indicated in the STEM image (inset). (b) EELS excitation maps at λ_0 = 650, 700, and 750 nm respectively. (c) E_z near-field images of the dimer from FDTD when excited by a vertical point dipole source 10 nm away from the apex. The driving field of the dipole has not been removed from the image so in order to see the induced fields on the dimer the colorscale has been saturated by a factor 300. Scale bars are 50 nm.